

Robust Hyperspectral Image Target Detection Using An Inequality Constraint

Shuo Yang, Zhenwei Shi, *Member, IEEE*, and Wei Tang

Abstract

In real hyperspectral images, there exist variations within spectra of materials. The inherent spectral variability is one of the major obstacles for the successful hyperspectral image target detection. Although several hyperspectral image target detection algorithms have been proposed, there are few algorithms considering the spectral variability. Under such circumstances, in this paper we propose a hyperspectral image target detection algorithm which is robust to the target spectral variability. The proposed algorithm utilizes an inequality constraint to guarantee that the outputs of target spectra which vary in a certain set are larger than one, so that these target spectra could be detected. The proposed algorithm transforms the target detection to a convex optimization problem and uses a kind of interior point method named barrier method to solve the formulated optimization problem effectively. Two synthetic hyperspectral images and two real hyperspectral images are used to conduct experiments. The experimental results demonstrate the proposed algorithm is robust to the target spectral variability and performs better than other classical algorithms.

Index Terms

Hyperspectral image, target detection, spectral variability, robust hyperspectral image target detection.

I. INTRODUCTION

The hyperspectral image, referred to as “data cube”, is a kind of three-dimensional datum with two spatial dimensions and one spectral dimension [1]. The hyperspectral imaging sensor provides each pixel a nearly continuous spectrum with dozens of or hundreds of very narrow bands (the width of each band is usually about 10 nm) [1]-[3].

The work was supported by the National Natural Science Foundation of China under the Grants 61273245 and 91120301, the Beijing Natural Science Foundation under the Grant 4152031, the Program for New Century Excellent Talents in University of Ministry of Education of China under the Grant NCET-11-0775, the funding project of State Key Laboratory of Virtual Reality Technology and Systems, Beihang University under the Grant VR-2014-ZZ-02, and the Fundamental Research Funds for the Central Universities under the Grant YWF-14-YHXY-028.

Shuo Yang is with Image Processing Center, School of Astronautics, Beihang University, Beijing 100191, P.R. China (E-mail: shuoyang@buaa.edu.cn).

Zhenwei Shi (Corresponding Author) is with Image Processing Center, School of Astronautics, Beihang University, Beijing 100191, PR China, with State Key Laboratory of Virtual Reality Technology and Systems, Beihang University, Beijing 100191, PR China and also with Beijing Key Laboratory of Digital Media, Beihang University, Beijing 100191, PR China (E-mail: shizhenwei@buaa.edu.cn).

Wei Tang is with Image Processing Center, School of Astronautics, Beihang University, Beijing 100191, P.R. China (E-mail: tangwei@sa.buaa.edu.cn).

In the hyperspectral image processing field, the hyperspectral image target detection is always a research focus because of its wide applications, such as mine detection [4], civilian search and rescue [5], gas-detection [6], and so on.

Several hyperspectral image target detection algorithms have been developed. Some hyperspectral image target detection algorithms are based on binary hypothesis testing, such as the famous adaptive matched filter (AMF) [1], [7], [8] and the adaptive coherence/cosine estimator (ACE) [1], [9]-[11]. AMF and ACE first assume the target and the background follow different probability models, then use the generalized-likelihood ratio test (GLRT) to obtain the detectors [1]. AMF and ACE are often applied using the local background statistics. The local adaptive version of AMF (L-AMF) and local adaptive version of ACE (L-ACE) use the dual window approach [12], in which the background statistics are calculated in an outer window. Another well known target detection algorithm is the constrained energy minimization (CEM) [13], [14]. CEM develops a finite impulse response (FIR) filter which minimizes the output energy under the constraint that the filter's response to the spectral signature of target is unity. CEM keeps the outputs of target pixels be large while suppressing the outputs of background pixels so that the target and the background can be separated. The spectral angle mapper (SAM) [15] algorithm measures the spectral angle between the test spectrum and the spectral signature of target. The spectral information divergence (SID) [16] algorithm uses the relative entropy to account for the spectral information and measures the probabilistic discrepancy between two spectra to compare the similarity of these two spectra.

The above mentioned algorithms all only need the prior knowledge of target's spectral signature. There are some algorithms that not only need the prior knowledge of target's spectral signature, but also need the prior knowledge of background's spectral signatures which is usually hard to obtain [17]. Orthogonal subspace projection (OSP) [18] is an example of such kind of algorithms. OSP first projects the test pixel's spectrum onto the orthogonal subspace of background signatures to eliminate the background signatures, and then finds a vector operator which maximizes the residual target signature signal-to-noise ratio (SNR). Recently, some sparse representation based target detection algorithms [19], [20] have been proposed. These algorithms need to build an overcomplete spectral dictionary which contains the spectral signatures of target and background and assume that the pixel's spectrum can be represented as a sparse linear combination of spectra contained in the overcomplete spectral dictionary. The sparse representation based target detection algorithms transform the target detection to an ℓ_0 norm minimization problem. But the choice of the spectral dictionary significantly affects the detection result of this kind of algorithm. In addition, the ℓ_0 norm minimization problem is hard to solve [21].

Several band selection algorithms have been proposed. In [22], Chang et al. explores the idea of CEM, and develops a linearly constrained minimum variance based constrained band selection (LCMV-CBS) algorithm. A problem of the band selection algorithm is how many bands should be selected. In [22], Chang et al. uses the virtual dimensionality (VD) [23] to determine the number of selected bands for LCMV-CBS. The target detection algorithms can be implemented after the band selection procedure. Another technology can be implemented before the target detection is the singular value decomposition (SVD) [24] in which the smaller singular values are removed, so that some noises and unwanted information can be removed.

One major obstacle for the hyperspectral image target detection is the inherent spectral variability [1]. Even in laboratory experiments, the same material can have different spectra because of the material surface variations [1]. In real hyperspectral remote sensing images, spectra of the same material can be different while spectra of different materials can be similar. Variations in atmospheric conditions, sensor noise, material composition, location and surrounding materials all can lead to spectral variability [1]. The spectral variability is an important cause of the false alarm and the miss detection. In the beamforming field, some researchers proposed a robust adaptive beamforming method [25] which uses worst-case performance optimization to solve the signal mismatch problem. In this paper, applying this robust adaptive beamforming method, we develop a hyperspectral image target detection algorithm which is robust to the spectral variability. The proposed algorithm minimizes the output energy and uses an inequality constraint to guarantee that the outputs of target spectra which vary in a certain set are larger than unity so that even if having some variations, these target spectra can still be detected. The proposed algorithm transforms the target detection to a convex optimization problem, which has the advantage that the local minimum is also the global minimum. Thus, we can use the optimization method to find the global minimum of the formulated optimization problem. In this paper, a kind of interior point method named barrier method [26] is utilized to solve the formulated optimization problem effectively. Two synthetic hyperspectral images and two real hyperspectral images are used to conduct experiments. The experiment results show the proposed algorithm performs better than other classical algorithms.

The rest of this paper is organized as follows. Some background knowledge is introduced in Section II. In Section III, we first propose our detection model, then solve it using the interior point method. Some theory analyses of the interior point method are also given in Section III. Section IV presents some experiment results and discussion. Finally some conclusions are drawn in Section V.

II. BACKGROUND

A pixel's spectrum of an N -pixel hyperspectral image with L bands can be represented in a vector form as $\mathbf{x}(n) = [x_1(n), \dots, x_L(n)]^T$ ($n = 1, \dots, N$), where T denotes matrix transpose. The spectral signature of target of interest can be represented as $\mathbf{d} = [d_1, \dots, d_L]^T$. \mathbf{d} can be obtained from the spectral library.

The CEM [13], [14] builds an FIR filter minimizing the total output energy subject to the constraint that the filter's response to \mathbf{d} is 1. Use $\mathbf{w} = [w_1, \dots, w_L]^T$ to denote the coefficients of the filter. $y(n) = \mathbf{w}^T \mathbf{x}(n)$ is the filter's output of the pixel $\mathbf{x}(n)$. The filter's average output energy is [1]:

$$\begin{aligned} E &= \frac{1}{N} \sum_{n=1}^N y^2(n) \\ &= \mathbf{w}^T \left[\frac{1}{N} \sum_{n=1}^N \mathbf{x}(n) \mathbf{x}^T(n) \right] \mathbf{w} \\ &= \mathbf{w}^T \hat{\mathbf{C}} \mathbf{w} \end{aligned} \tag{1}$$

where $\hat{\mathbf{C}} = \frac{1}{N} \sum_{n=1}^N \mathbf{x}(n) \mathbf{x}^T(n)$ is the estimated correlation matrix. The CEM finds an optimal \mathbf{w} by solving the

following constrained optimization problem [1]:

$$\begin{aligned} & \min_{\mathbf{w}} \mathbf{w}^T \hat{\mathbf{C}} \mathbf{w} \\ & \text{s.t. } \mathbf{w}^T \mathbf{d} = 1 \end{aligned} \quad (2)$$

(2) can be solved by using the Lagrange multiplier method [27]. The solution of (2) is [1]:

$$\mathbf{w}_{CEM} = \frac{\hat{\mathbf{C}}^{-1} \mathbf{d}}{\mathbf{d}^T \hat{\mathbf{C}}^{-1} \mathbf{d}} \quad (3)$$

For the pixel $\mathbf{x}(n)$, the output of the CEM is [1]:

$$y_{CEM}(\mathbf{x}) = \mathbf{w}_{CEM}^T \mathbf{x} = \frac{\mathbf{d}^T \hat{\mathbf{C}}^{-1} \mathbf{x}}{\mathbf{d}^T \hat{\mathbf{C}}^{-1} \mathbf{d}} \quad (4)$$

III. PROPOSED ALGORITHM

In this section, we first propose our robust hyperspectral image target detection model, then solve it using a kind of interior point method named barrier method [26]. We also give some theory analyses of the barrier method in this section.

A. Formulation

In the real hyperspectral image, there is spectral variability within the target of interest. This variability is one of the major obstacles for the successful target detection. Thus it is useful to develop a hyperspectral image target detection algorithm which is robust to spectral variability. In this paper, applying the robust adaptive beamforming method [25], we develop a hyperspectral image target detection algorithm which is robust to the target spectral variability.

Suppose the target pixels' spectra vary in a sphere with the radius $\varepsilon > 0$. Thus, the actual target pixels' spectra belong to the set

$$\mathcal{A}(\varepsilon) = \{ \mathbf{c} \mid \mathbf{c} = \mathbf{d} + \mathbf{e}, \|\mathbf{e}\| \leq \varepsilon \} \quad (5)$$

where \mathbf{c} denotes the actual target spectrum, and \mathbf{e} denotes the spectral variation, and $\|\cdot\|$ denotes the Euclidean norm. Like the CEM, we also develop an FIR filter, and let $\mathbf{w} = [w_1, \dots, w_L]^T$ denote the coefficients of the filter. For CEM, the constraint $\mathbf{w}^T \mathbf{d} = 1$ constrains the output of \mathbf{d} to be 1. In our proposed algorithm, considering the spectral variability, we constrain that the outputs of all spectra in the set \mathcal{A} are not smaller than 1. At the same time, we minimize the output energy. Thus the proposed algorithm can be formulated as the following constrained optimization problem:

$$\begin{aligned} & \min_{\mathbf{w}} \mathbf{w}^T \hat{\mathbf{C}} \mathbf{w} \\ & \text{s.t. } \mathbf{w}^T \mathbf{c} \geq 1 \text{ for all } \mathbf{c} \in \mathcal{A} \end{aligned} \quad (6)$$

In the beamforming field, (6) is used to solve the signal mismatch problem, but in that case, a complex form formula is used [25]. The inequality constraint in (6) guarantees that even the target spectra have some variations, (i.e., in the set \mathcal{A}), the outputs of these target spectra will be larger than 1. At the same time, minimizing the output energy

can suppress the outputs of background. Therefore, (6) should improve the detection result when there is spectral variability within target.

Because of the spectral variability, different materials may have similar spectra. The set $\mathcal{A}(\varepsilon)$ in (5) may also contain some background pixels whose spectra are similar with the spectral signature of target \mathbf{d} . (6) may enlarge the output of this kind of background pixels. However, a spectrum in $\mathcal{A}(\varepsilon)$ is most likely to belong to a target pixel. This is because that the parameter ε is usually set to small values, and the spectrum \mathbf{c} in $\mathcal{A}(\varepsilon)$ is similar with the spectral signature of target \mathbf{d} . The set $\mathcal{A}(\varepsilon)$ in fact is a ball centered at \mathbf{d} with radius ε . Since ε is usually small, the spectra in $\mathcal{A}(\varepsilon)$ are more likely to belong to target pixels. CEM uses the constraint $\mathbf{w}^T \mathbf{d} = 1$. So when minimize the output energy $\mathbf{w}^T \hat{\mathbf{C}} \mathbf{w}$, the outputs of those targets' spectra which are similar with \mathbf{d} but not equal to \mathbf{d} will also be suppressed. We use the inequality constraint $\mathbf{w}^T \mathbf{c} \geq 1$ for all $\mathbf{c} \in \mathcal{A}$ to guarantee that all the spectra in $\mathcal{A}(\varepsilon)$ have large outputs, at the same time we minimize the output energy $\mathbf{w}^T \hat{\mathbf{C}} \mathbf{w}$. And because the spectra in $\mathcal{A}(\varepsilon)$ are more likely to belong to target pixels, minimizing the output energy will suppress the outputs of background pixels more heavily and the target pixels' outputs and the background pixels' outputs will be more separable. Thus, although (6) may increase the false alarm rate, (6) should give a greater increase degree of target detection rate compared with other classical algorithms. For the classical algorithms, like CEM and ACE, one can set low thresholds to detection outputs to get target detection binary maps with high target detection rates but also high false alarm rates. But the proposed algorithm (6) should get a higher target detection rate under the same false alarm rate. The experimental results also confirm this. Another point to note is that if we want to guarantee that the target spectra varying in a certain range can be detected while regardless the false alarm rate, due to the constraint in (6), we can set a corresponding ε and directly set the threshold to 1 to get a detection binary map. So the target spectra which vary in the set $\mathcal{A}(\varepsilon)$ must can be detected in the detection binary map. In addition, under some circumstances, if we know exactly the target spectra varying range, we can directly set a corresponding ε to guarantee the target spectra can be detected. Our algorithm uses the inequality constraint to explicitly guarantee that the target spectra which vary in $\mathcal{A}(\varepsilon)$ must have outputs that are larger than 1. This is a big difference with other algorithms.

According to (5), (6) is equivalent to

$$\begin{aligned} & \min_{\mathbf{w}} \mathbf{w}^T \hat{\mathbf{C}} \mathbf{w} \\ \text{s.t. } & \mathbf{w}^T \mathbf{d} + \mathbf{w}^T \mathbf{e} \geq 1 \text{ for all } \|\mathbf{e}\| \leq \varepsilon \end{aligned} \quad (7)$$

We have that $\mathbf{w}^T \mathbf{e} \geq -\|\mathbf{w}\| \|\mathbf{e}\| \geq -\varepsilon \|\mathbf{w}\|$ for all $\|\mathbf{e}\| \leq \varepsilon$. The equalities hold when $\|\mathbf{e}\| = \varepsilon$ and \mathbf{e} has the opposite direction with \mathbf{w} . Thus the minimum element of $\mathbf{w}^T \mathbf{d} + \mathbf{w}^T \mathbf{e}$ for all $\|\mathbf{e}\| \leq \varepsilon$ is $\mathbf{w}^T \mathbf{d} - \varepsilon \|\mathbf{w}\|$. We can rewrite (7) equivalently as:

$$\begin{aligned} & \min_{\mathbf{w}} f_0(\mathbf{w}) = \mathbf{w}^T \hat{\mathbf{C}} \mathbf{w} \\ \text{s.t. } & 1 + \varepsilon \|\mathbf{w}\| - \mathbf{w}^T \mathbf{d} \leq 0 \end{aligned} \quad (8)$$

The optimization problem (8) has no closed form solution, and the solution must be obtained through iteration. In this paper, we use an interior point method named barrier method [26] to solve the problem (8). By making the

inequality constraint implicit in the objective function, (8) can be rewritten as follows:

$$\min_{\mathbf{w}} \mathbf{w}^T \hat{\mathbf{C}} \mathbf{w} + I_-(1 + \varepsilon \|\mathbf{w}\| - \mathbf{w}^T \mathbf{d}) \quad (9)$$

where $I_-: \mathbf{R} \rightarrow \mathbf{R}$ is the indicator function for the nonpositive reals [26],

$$I_-(u) = \begin{cases} 0 & u \leq 0 \\ \infty & u > 0 \end{cases} \quad (10)$$

The indicator function I_- can be approximated by the following function [26]:

$$\hat{I}_-(u) = -(1/t) \log(-u) \quad (11)$$

where $t > 0$ sets the accuracy of the approximation. As t increases, the approximation accuracy increases. Unlike I_- which is not differentiable, \hat{I}_- is differentiable. Substituting \hat{I}_- for I_- , we can get the approximation of (9) as:

$$\min_{\mathbf{w}} \mathbf{w}^T \hat{\mathbf{C}} \mathbf{w} - (1/t) \log(\mathbf{w}^T \mathbf{d} - \varepsilon \|\mathbf{w}\| - 1) \quad (12)$$

The objective function in (12) is convex and differentiable. The function

$$\phi(\mathbf{w}) = -\log(\mathbf{w}^T \mathbf{d} - \varepsilon \|\mathbf{w}\| - 1) \quad (13)$$

is called the logarithmic barrier or log barrier of (8) [26]. (12) is equivalent to the following problem:

$$\min_{\mathbf{w}} f_1(\mathbf{w}) = t \mathbf{w}^T \hat{\mathbf{C}} \mathbf{w} - \log(\mathbf{w}^T \mathbf{d} - \varepsilon \|\mathbf{w}\| - 1) \quad (14)$$

$f_1(\mathbf{w})$ is a convex function, and (14) can be solved by using the Newton's method [26], [27]. Use $\mathbf{w}^*(t)$ to denote the solution of (14) with the parameter t , and use p^* to denote the optimal value of the original problem (8). It can be proved that [26]

$$f_0(\mathbf{w}^*(t)) - p^* \leq 1/t \quad (15)$$

Thus as $t \rightarrow \infty$, $\mathbf{w}^*(t)$ converges to the optimal point of the original problem (8).

The barrier method [26] is a kind of interior point method. The basic idea of the barrier method is: increase t and solve the corresponding problem (14) repeatedly so that the solution of (14) tends to the optimal point of the original problem (8) as t increases. Algorithm 1 gives the barrier method for the proposed model (8). In this paper, we set $\mu_1 = 10$, $\mu_2 = 0.1$, $\epsilon_1 = 10^{-6}$ and $\epsilon_2 = 10^{-4}$. We initialize $t = 10^{-2}$ in step 1 of Algorithm 1. In a practical implementation, in step 5, if $\mathbf{w} - \mu_2 \nabla^2 f_1(\mathbf{w})^{-1} \nabla f_1(\mathbf{w}) \notin \text{dom} f_1$, we multiply μ_2 by 0.1 until $\mathbf{w} - \mu_2 \nabla^2 f_1(\mathbf{w})^{-1} \nabla f_1(\mathbf{w}) \in \text{dom} f_1$, where $\text{dom} f_1$ denotes the domain of $f_1(\mathbf{w})$. After getting the solution of (8): \mathbf{w}^* , we project the pixels' spectra $\mathbf{x}(n)$ ($n = 1, \dots, N$) to \mathbf{w}^* and get the outputs of the proposed algorithm:

$$y(n) = \mathbf{w}^{*T} \mathbf{x}(n) \quad n = 1, \dots, N \quad (16)$$

A threshold η can be set. If $y(n) > \eta$, the pixel is labeled as a target pixel; else the pixel is labeled as a background pixel.

Algorithm 1 Barrier method for the robust target detection algorithm**Initialization:**

- 1: Select a strictly feasible \mathbf{w} that satisfies $1 + \varepsilon \|\mathbf{w}\| - \mathbf{w}^T \mathbf{d} < 0$.
Set $t > 0$, $\mu_1 > 1$, $0 < \mu_2 < 1$, tolerance $\epsilon_1 > 0$ and tolerance $\epsilon_2 > 0$.

Main iteration:**Subiteration (solving (14) by applying the Newton's method):**

- 2: Use \mathbf{w} as the start point.

- 3: Set $\mathbf{w}_{old} = \mathbf{w}$.

- 4: Compute the gradient and the Hessian matrix of (14):

$$\begin{aligned}\nabla f_1(\mathbf{w}) &= 2t\hat{\mathbf{C}}\mathbf{w} + \frac{1}{\mathbf{w}^T \mathbf{d} - \varepsilon \|\mathbf{w}\| - 1} (\varepsilon \frac{\mathbf{w}}{\|\mathbf{w}\|} - \mathbf{d}) \\ \nabla^2 f_1(\mathbf{w}) &= 2t\hat{\mathbf{C}} + \frac{1}{(\mathbf{w}^T \mathbf{d} - \varepsilon \|\mathbf{w}\| - 1)^2} (\varepsilon \frac{\mathbf{w}}{\|\mathbf{w}\|} - \mathbf{d})(\varepsilon \frac{\mathbf{w}}{\|\mathbf{w}\|} - \mathbf{d})^T \\ &\quad + \frac{\varepsilon}{\mathbf{w}^T \mathbf{d} - \varepsilon \|\mathbf{w}\| - 1} \left(\frac{\mathbf{I}}{\|\mathbf{w}\|} - \frac{\mathbf{w}\mathbf{w}^T}{\|\mathbf{w}\|^3} \right)\end{aligned}$$

- 5: Update $\mathbf{w} \leftarrow \mathbf{w} - \mu_2 \nabla^2 f_1(\mathbf{w})^{-1} \nabla f_1(\mathbf{w})$

Stop subiteration if $\|\mathbf{w} - \mathbf{w}_{old}\| < \epsilon_2$, and get $\mathbf{w}^*(t) = \mathbf{w}$;

else go to step 3.

Stop main iteration if $1/t < \epsilon_1$;

else increase $t = \mu_1 t$, and go to step 2.

B. Theory Analysis

Theorem 1. The Algorithm 1 can achieve the desired accuracy ϵ_1 after $\frac{\log(1/(\epsilon_1 t^0))}{\log \mu_1}$ times main iteration, where t^0 is the initial value of t [26].

Proof: The Hessian matrix of $f_1(\mathbf{w})$ in (14) is:

$$\begin{aligned}\nabla^2 f_1(\mathbf{w}) &= 2t\hat{\mathbf{C}} + \frac{\varepsilon}{\mathbf{w}^T \mathbf{d} - \varepsilon \|\mathbf{w}\| - 1} \left(\frac{\mathbf{I}}{\|\mathbf{w}\|} - \frac{\mathbf{w}\mathbf{w}^T}{\|\mathbf{w}\|^3} \right) \\ &\quad + \frac{1}{(\mathbf{w}^T \mathbf{d} - \varepsilon \|\mathbf{w}\| - 1)^2} (\varepsilon \frac{\mathbf{w}}{\|\mathbf{w}\|} - \mathbf{d})(\varepsilon \frac{\mathbf{w}}{\|\mathbf{w}\|} - \mathbf{d})^T\end{aligned}\tag{17}$$

For the hyperspectral image, the estimated correlation matrix $\hat{\mathbf{C}}$ is usually a positive definite matrix. $(\varepsilon \frac{\mathbf{w}}{\|\mathbf{w}\|} - \mathbf{d})(\varepsilon \frac{\mathbf{w}}{\|\mathbf{w}\|} - \mathbf{d})^T$ is a positive semidefinite matrix. For any non-zero vector \mathbf{z} , we have that:

$$\mathbf{z}^T \left(\frac{\mathbf{I}}{\|\mathbf{w}\|} - \frac{\mathbf{w}\mathbf{w}^T}{\|\mathbf{w}\|^3} \right) \mathbf{z} = \frac{\|\mathbf{z}\|^2 \|\mathbf{w}\|^2 (1 - \cos^2 \theta)}{\|\mathbf{w}\|^3} \geq 0\tag{18}$$

where θ is the angle between \mathbf{w} and \mathbf{x} . (18) shows $\frac{\mathbf{I}}{\|\mathbf{w}\|} - \frac{\mathbf{w}\mathbf{w}^T}{\|\mathbf{w}\|^3}$ is a positive semidefinite matrix. Noticing $\mathbf{w}^T \mathbf{d} - \varepsilon \|\mathbf{w}\| - 1 > 0$, it is can be seen that $\nabla^2 f_1(\mathbf{w})$ is a positive definite matrix. Thus the objective function $f_1(\mathbf{w})$ in (14) is a convex function, and (14) is a convex optimization problem. Using the Taylor formula, we have that:

$$\begin{aligned}f_1(\mathbf{w} - \mu_2 \nabla^2 f_1(\mathbf{w})^{-1} \nabla f_1(\mathbf{w})) \\ = f_1(\mathbf{w}) - \mu_2 \nabla^T f_1(\mathbf{w}) \nabla^2 f_1(\mathbf{w})^{-1} \nabla f_1(\mathbf{w}) + o(\mu_2)\end{aligned}\tag{19}$$

Since $\nabla^2 f_1(\mathbf{w})$ is positive definite, $\nabla^2 f_1(\mathbf{w})^{-1}$ is also positive definite. If \mathbf{w} is not the minimum point, $\nabla^T f_1(\mathbf{w}) \nabla^2 f_1(\mathbf{w})^{-1} \nabla f_1(\mathbf{w}) > 0$. Thus if μ_2 is small enough, the step 5 in Algorithm 1 can make the objective function $f_1(\mathbf{w})$ in (14) descent. Because $f_1(\mathbf{w})$ is a convex function, the subiteration in Algorithm 1 can converge

to the global minimum of the optimization problem (14). Utilizing (15), we can conclude that after

$$\frac{\log(1/(\epsilon_1 t^0))}{\log \mu_1} \quad (20)$$

[26] times main iteration the Algorithm 1 can achieve the desired accuracy ϵ_1 , where t^0 is the initial value of t . ■

Next, we give the computational complexity of the proposed algorithm. The time complexity of calculating the estimated correlation matrix $\hat{\mathbf{C}}$ is $O(NL^2)$. Both the time complexities of calculating $\nabla f_1(\mathbf{w})$ and $\nabla^2 f_1(\mathbf{w})$ are $O(L^2)$, and the time complexity of calculating $\nabla^2 f_1(\mathbf{w})^{-1}$ is $O(L^3)$. After knowing the $\nabla^2 f_1(\mathbf{w})^{-1}$, the time complexity of calculating $\nabla^2 f_1(\mathbf{w})^{-1} \nabla f_1(\mathbf{w})$ is $O(L^2)$. The total time complexity for the proposed algorithm is $O(NL^2 + L^3)$.

IV. EXPERIMENT RESULTS AND DISCUSSION

In this section, we use two synthetic hyperspectral images and two real hyperspectral images to conduct experiments. The proposed algorithm is compared with some classical algorithms including CEM, SAM, SID, ACE, AMF, L-ACE and L-AMF. We also implement CEM after the SVD processing, in which only these singular values which make up 90% of all singular values' energy are retained. The LCMV-CBS is used to implement the band selection, and then the SAM is conducted on the selected bands. The number of selected bands is determined by the VD where the false alarm probability in the VD procedure equals 10^{-4} as does in [22]. The above mentioned LCMV-CBS based SAM (LCMV-CBS-SAM) and the SVD based CEM (SVD-CEM) are also compared with our proposed algorithm. In the experiments all of the algorithms only need the prior knowledge of the target's spectral signature. In the experiments, receiver operating characteristic (ROC) curves [1], [28], [29] are used to evaluate the algorithms. Based on ground truth, the ROC curve plots the varying relationship between the false alarm rate (F_a) and the probability of detection (P_d). The definitions of F_a and P_d are:

$$F_a = \frac{N_f}{N}, \quad P_d = \frac{N_c}{N_t} \quad (21)$$

where N_f is the number of false alarm pixels, N is the total number of the hyperspectral image pixels, N_c is the number of correct detection target pixels, and N_t is the number of total true target pixels. The sizes of inner windows and outer windows for the L-ACE and the L-AMF are selected as follows: in the two synthetic hyperspectral image experiments and in the real hyperspectral image experiment 1, for the size of inner window, we try all the odd numbers in [1, 19], and for the size of outer window, we try all the odd numbers in [1, 39]. Note that the size of outer window must be larger than the size of inner window. Then, in this paper, among all the tried window sizes, we report the performances which have the largest areas under the ROC curves. For the real hyperspectral image experiment 2, we will introduce the window size selected method in Section IV D. When we calculate the inverse of local covariance matrix in L-ACE and L-AMF, we add a small value 0.001 to the diagonal elements of the local covariance matrix, so that the stability of the inverse of the local covariance matrix can be improved [30], [31].

A. Synthetic Hyperspectral Image Experiment 1

We use the method which is similar to that introduced by Chang et al. [32] to design a synthetic hyperspectral image. We choose five pure pixels' spectra: airplane (A), roof (R), grass (G), parking apron (P) and ground (Gd) from a real airborne visible/infrared imaging spectrometer (AVIRIS) hyperspectral image. The scene of the real hyperspectral image is the San Diego airport, San Diego, USA. The mean of the real hyperspectral image denoted by M is also calculated. After removing low SNR and water absorption bands, A, G, R, P, Gd and M have 189 bands left, and the spectral range is 0.4-2.5 μm . We normalize the spectra of A, G, R, P, Gd and M to [0, 1] as shown in Fig. 1. These six spectra are used to design a synthetic hyperspectral image with 200×200 pixels. Fig. 2 shows the first band of the synthetic hyperspectral image. Some panels whose value in band 1 are similar with the background cannot be distinguished from background in Fig. 2. In this synthetic hyperspectral image, there are 25 panels arranged in a 5×5 matrix. In column 1, there are five 4×4 panels, and in column 2, there are five 2×2 panels. Both in column 1 and column 2, from top to bottom, the panels are simulated by spectra of A, R, G, P and Gd, respectively. In column 3, there are five 2×2 panels, and the simulated methods of each pixel are given in Table I. Both in column 4 and column 5, there are five 1×1 panels, and the panels are simulated as mix-pixels. In column 4, from top to bottom, the panels are simulated by: $0.5A + 0.5M$, $0.5R + 0.5M$, $0.5G + 0.5M$, $0.5P + 0.5M$ and $0.5Gd + 0.5M$, respectively. In column 5, from top to bottom, the panels are simulated by: $0.75A + 0.25M$, $0.75R + 0.25M$, $0.75G + 0.25M$, $0.75P + 0.25M$ and $0.75Gd + 0.25M$, respectively. The background pixels are simulated using the linear mixing model [33]. The R, G, P, Gd and M are used as background endmembers. For each background pixel, the abundances of R, G, P, Gd and M are generated randomly. The abundances satisfy the nonnegativity constraint and the sum-to-one constraint. We add the additive Gaussian white noise to the synthetic hyperspectral image to achieve a 50 dB SNR.

TABLE I
THE SIMULATED METHODS OF EACH PIXEL IN COLUMN 3 OF THE SYNTHETIC HYPERSPECTRAL IMAGE 1

	pixel 1	pixel 2	pixel 3	pixel 4
panel 1	$0.5A + 0.5R$	$0.5A + 0.5G$	$0.5A + 0.5P$	$0.5A + 0.5Gd$
panel 2	$0.5R + 0.5A$	$0.5R + 0.5G$	$0.5R + 0.5P$	$0.5R + 0.5Gd$
panel 3	$0.5G + 0.5A$	$0.5G + 0.5R$	$0.5G + 0.5P$	$0.5G + 0.5Gd$
panel 4	$0.5P + 0.5A$	$0.5P + 0.5R$	$0.5P + 0.5G$	$0.5P + 0.5Gd$
panel 5	$0.5Gd + 0.5A$	$0.5Gd + 0.5R$	$0.5Gd + 0.5G$	$0.5Gd + 0.5P$

We use this synthetic hyperspectral image to detect the target A, because the other five spectra are contained in every background pixel. A has 30 target pixels. In order to evaluate the algorithms' detection results when there is spectral variability within the target, when the endmember A is used to simulate pixels, we add random vectors which have unity norms to the endmembers A. Fig. 3 shows five example spectra of target A contained pixels. From Fig. 3, we can see the target spectral variability in this synthetic hyperspectral image. The ground truth of the target A is shown in Fig. 4. The spectrum of A shown in Fig. 1 is used as the spectral signature of target for

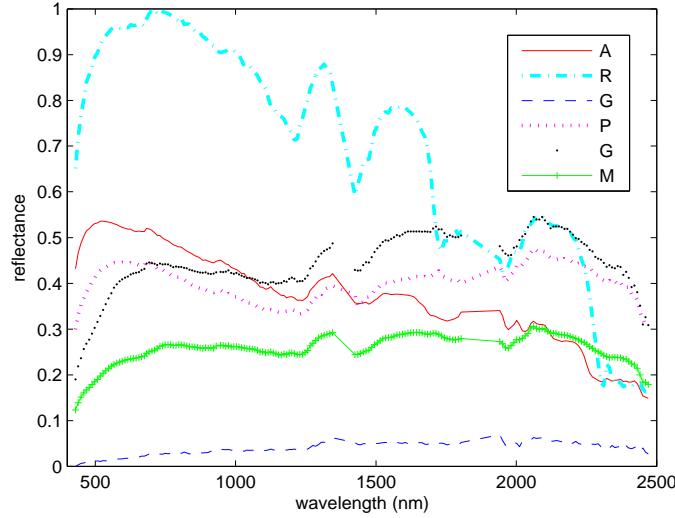


Fig. 1. Spectra of A, G, R, P, Gd and M.

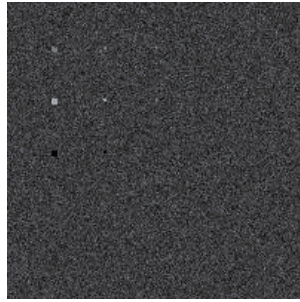


Fig. 2. The first band of the synthetic hyperspectral image 1.

all the algorithms. The ε in the proposed algorithm is set to 0.1. The detection results of different algorithms are shown in Fig. 5. Since Fig. 5 is not clear to see, we show the false alarm rates of different algorithms when the probabilities of detection reach 1 in Table II. Table II shows our algorithm has the smallest false alarm rate. ROC curves of different algorithms are shown in Fig. 6. The ROC curves also demonstrate that our proposed algorithm performs better than the other algorithms. The experiment results show that the proposed algorithm is more robust to the spectral variability within this synthetic hyperspectral image and can obtain better detection results.

TABLE II

THE FALSE ALARM RATES OF DIFFERENT ALGORITHMS WHEN THE PROBABILITIES OF DETECTION REACH 1 FOR THE SYNTHETIC HYPERSPECTRAL IMAGE 1

	our algorithm	CEM	ACE	AMF	L-ACE	L-AMF	SAM	SID	LCMV-CBS-SAM	SVD-CEM
false alarm rate	0	0.4680	0.9992	0.9992	0.6344	0.3189	0.6000	0.6790	0.7418	0.9972

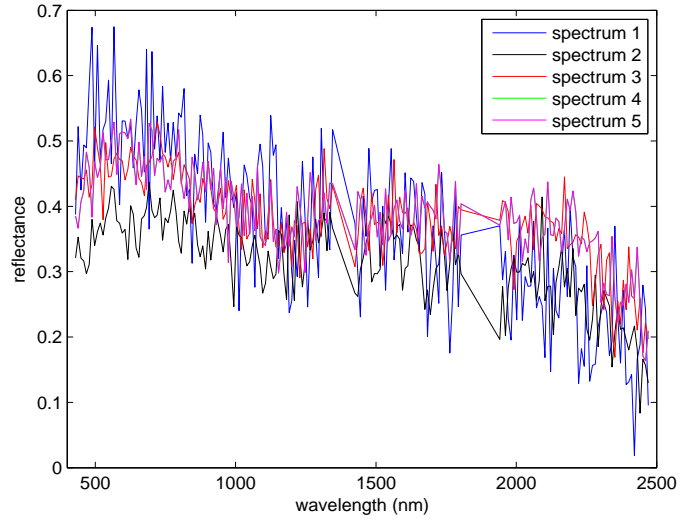


Fig. 3. Five example spectra of the target A in the synthetic hyperspectral image 1.



Fig. 4. The ground truth of the target A in the synthetic hyperspectral image 1.

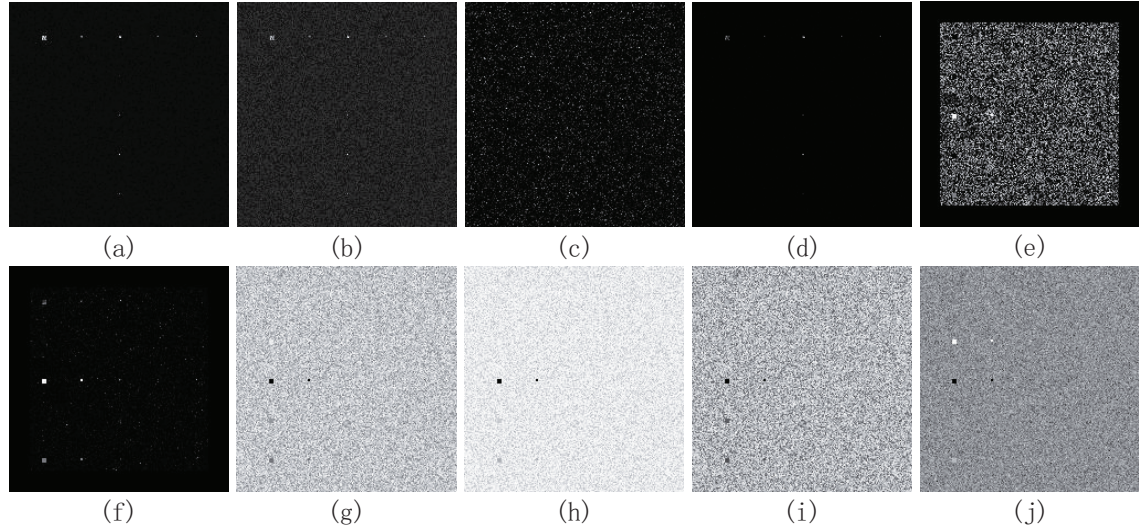


Fig. 5. The output detection results of the synthetic hyperspectral image 1: (a) our algorithm, (b) CEM, (c) ACE, (d) AMF, (e) L-ACE, (f) L-AMF, (g) SAM, (h) SID, (i) LCMV-CBS-SAM (j) SVD-CEM.

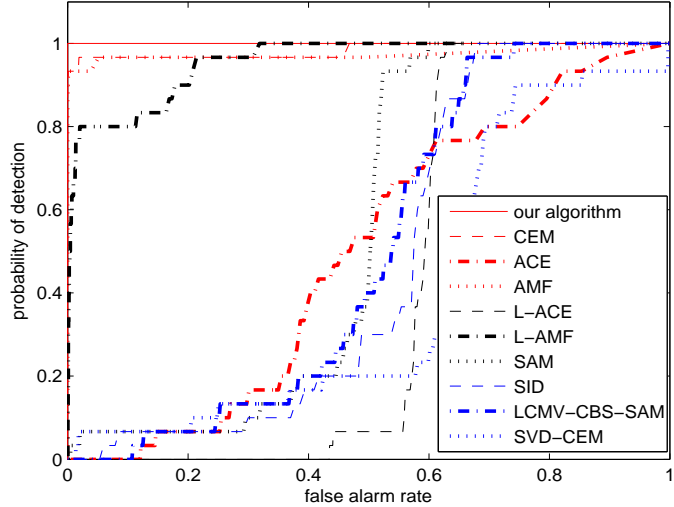


Fig. 6. ROC curves of different algorithms for the synthetic hyperspectral image 1.

B. Synthetic Hyperspectral Image Experiment 2

In this subsection, we use another synthetic hyperspectral image to evaluate the algorithms. The generation process of the synthetic data is similar to that in [34]. 15 kinds of spectral signatures are chosen from the United States Geological Survey (USGS) [35] Digital Spectral Library to generate our synthetic data. The 15 kinds of endmember signatures used for our synthetic experiments are: Axinite HS342.3B, Rhodochrosite HS67, Chrysocolla HS297.3B, Niter GDS43 (K-Saltpeter), Anthophyllite HS286.3B, Neodymium Oxide GDS34, Monazite HS255.3B, Samarium Oxide GDS36, Pigeonite HS199.3B, Meionite WS700.HLsep, Spodumene HS210.3B, Labradorite HS17.3B, Grossular WS484, Zoisite HS347.3B and Wollastonite HS348.3B. The reflectance values of the 15 kinds of materials are measured for 224 spectral bands distributed uniformly in the interval $0.4 - 2.5 \mu\text{m}$.

The synthetic data are created as follows:

- 1) Divide the scene, whose size is $s^2 \times s^2$ ($s = 8$), into $s \times s$ regions. Initialize each region with the same type of ground cover, randomly selected from the endmember class. The total number of endmembers is P ($P = 15$). The size of spectral signatures matrix \mathbf{W} is $L \times P$ ($L = 224$).
- 2) Generate mixed pixels through a simple $(s + 1) \times (s + 1)$ mean filter. I.e., for a pixel, we calculate its $(s + 1) \times (s + 1) - 1$ neighborhood pixels' mean and use the mean to replace the pixel's value.
- 3) Replace all the pixels in which the abundance of a single endmember is larger than 70% with a mixture made up of only two endmembers (the abundances of the two endmembers both equal 50%) so as to further remove pure pixels. The two endmembers used to substitute the original endmember are the original endmember whose abundance is larger than 70% and its next endmember. For example, if in a pixel, the abundance of the 1st endmember is larger than 70%, the pixel will be replaced with a mixture made up of the 1st endmember and the 2nd endmember (the abundances of these two endmembers both equal 50%). If in a

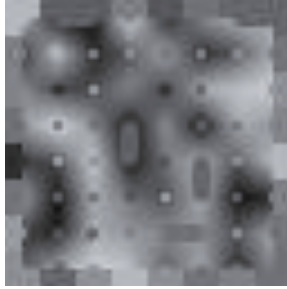


Fig. 7. The first band of the synthetic hyperspectral image 2.



Fig. 8. The ground truth of the Axinite HS342.3B target in the synthetic hyperspectral image 2.

pixel, the abundance of the 15th endmember is larger than 70%, the pixel will be replaced with a mixture made up of the 15th endmember and the 1st endmember (the abundances of these two endmembers both equal 50%). Now, we have the distribution of P endmembers in the scene and the corresponding abundance values which are stored in \mathbf{H} with a size of $P \times K$ ($K = s^2 \times s^2$).

- 4) Use linear spectral mixing model $\mathbf{Y} = \mathbf{W} \times \mathbf{H}$ to generate hyperspectral data. The size of hyperspectral data matrix \mathbf{Y} is $L \times K$.

Note that there is no pure pixel in this synthetic hyperspectral image. Fig. 7 shows the first band of the synthetic hyperspectral image. We use this synthetic hyperspectral image to detect the Axinite HS342.3B target as example. The total number of target pixels is 790. Fig. 8 shows the ground truth of the Axinite HS342.3B target. The spectrum of the Axinite HS342.3B in the USGS Digital Spectral Library as shown in Fig. 9 is used as the spectral signature of target in the experiments. We plot five example spectra of the target pixels in Fig. 10. From Fig. 10, we can see that because of the existence of mixed pixels, there are some target spectral variations in this synthetic data. In this experiment, the ε used in the proposed algorithm is set to 0.1. The output detection results of different algorithms are shown in Fig. 11. The ROC curves of different algorithms are shown in Fig. 12. The ROC curves denote our algorithm outperforms than the other algorithms. This experiment result indicates that when the synthetic hyperspectral data contain the mixed pixel target which can cause the spectral variation, the proposed algorithm is more robust.

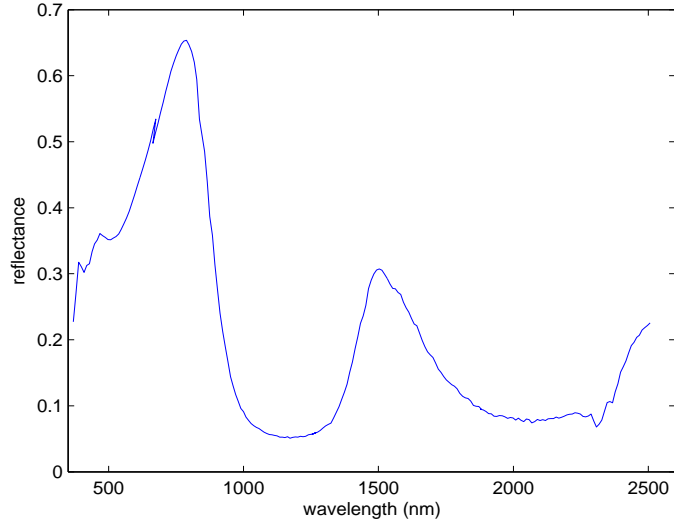


Fig. 9. Spectral signature of target used in the synthetic hyperspectral image 2 experiment.

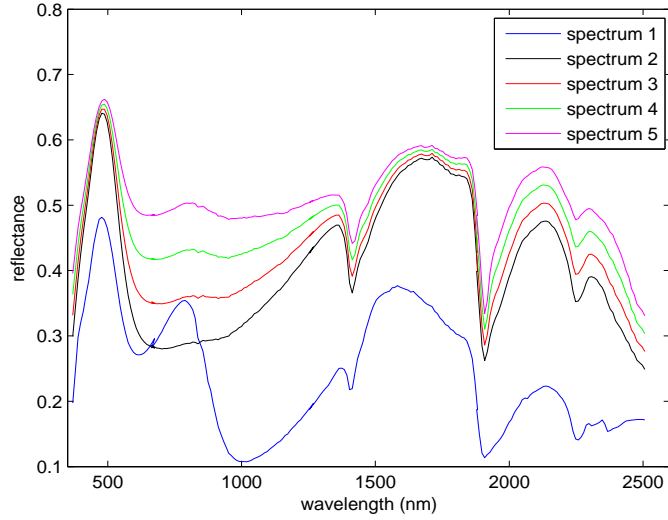


Fig. 10. Five example spectra of the Axinite HS342.3B target in the synthetic hyperspectral image 2.

C. Real Hyperspectral Image Experiment 1

In this subsection, a real Cuprite hyperspectral image [36] collected by AVIRIS is used to do experiments. AVIRIS collected hyperspectral data in 224 bands and the spectral range is 0.4–2.5 μm . The experimental data have 250×191 pixels. We have removed the low SNR and water absorption bands, and 188 bands are left. Fig. 13 shows the first band of the experimental AVIRIS hyperspectral image. This AVIRIS hyperspectral image is used to detect the buddingtonite target, which totally has 39 pixels. The ground truth [37] of the buddingtonite target is shown in Fig. 14. There are two buddingtonite spectra in the USGS Digital Spectral Library [35]. The mean of

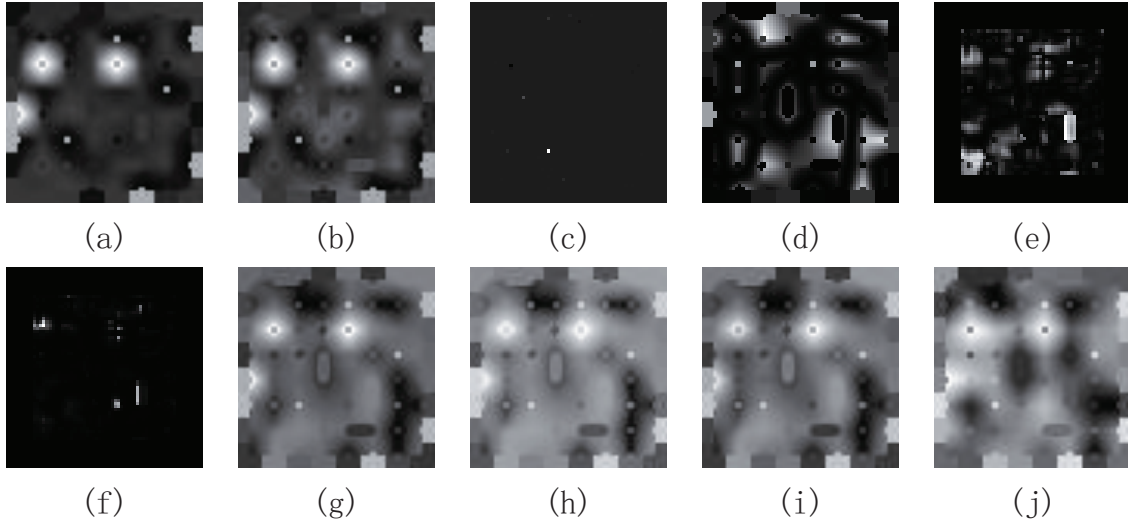


Fig. 11. The output detection results of the synthetic hyperspectral image 2: (a) our algorithm, (b) CEM, (c) ACE, (d) AMF, (e) L-ACE, (f) L-AMF, (g) SAM, (h) SID, (i) LCMV-CBS-SAM (j) SVD-CEM.

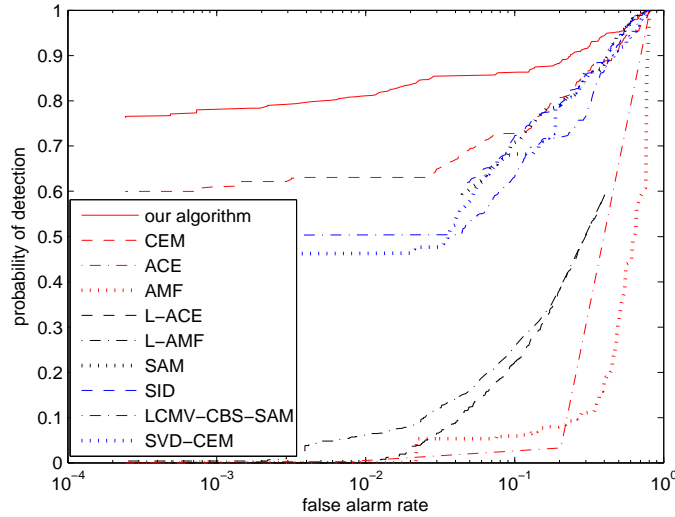


Fig. 12. ROC curves of different algorithms for the synthetic hyperspectral image 2.

these two buddingtonite spectra as shown in Fig. 15 is used as the spectral signature of target for all algorithms. Fig. 16 shows the spectra of target pixels in the experimental AVIRIS hyperspectral image. From Fig. 16, we can see that spectra of the same target are not identical. There indeed exists spectral variability for the target in real hyperspectral image.

In the experiment, ε used in the proposed algorithm is set to 0.1. Fig. 17 shows the output detection results of different algorithms. By setting suitable thresholds, we transform the detection results to binary images as shown in Fig. 18, where the detection probabilities of different algorithms are all 0.5. From Fig. 18 we can see that under

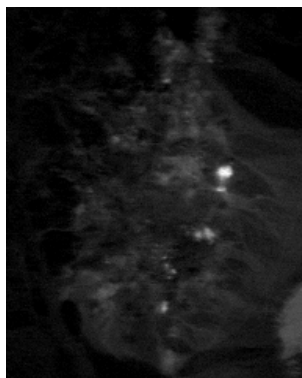


Fig. 13. The first band of the AVIRIS hyperspectral image.

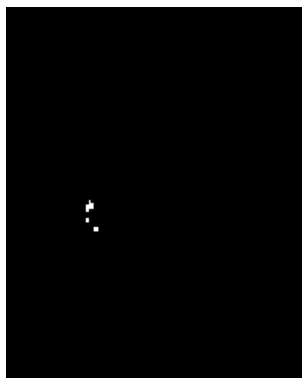


Fig. 14. The ground truth of the buddingtonite target in the AVIRIS hyperspectral image.

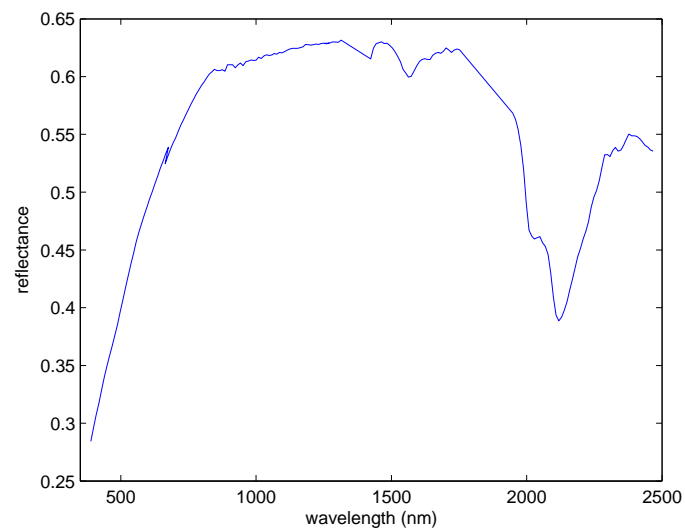


Fig. 15. Spectral signature of target used in the AVIRIS hyperspectral image experiment.

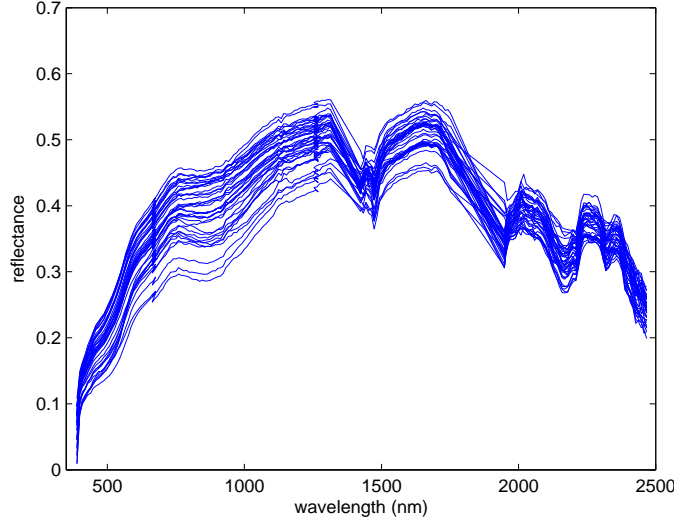


Fig. 16. Spectral variability of target in the AVIRIS hyperspectral image.

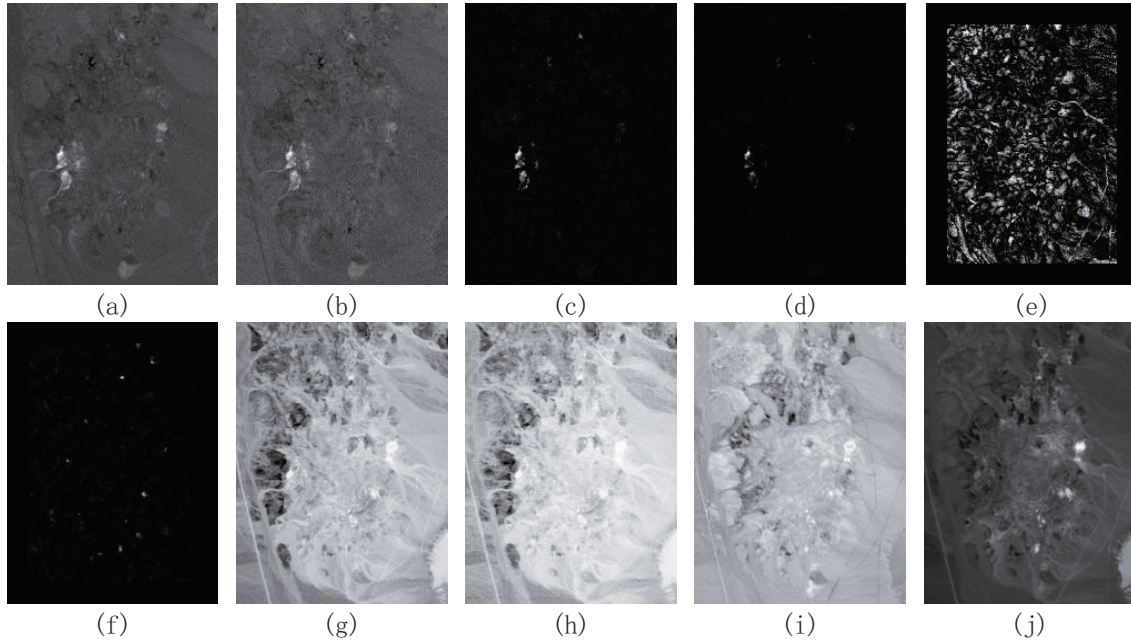


Fig. 17. The output detection results of the AVIRIS hyperspectral image: (a) our algorithm, (b) CEM, (c) ACE, (d) AMF, (e) L-ACE, (f) L-AMF, (g) SAM, (h) SID, (i) LCMV-CBS-SAM (j) SVD-CEM.

the same detection probabilities, the false alarm pixels of the proposed algorithm are much fewer than the other algorithms. We plot the ROC curves of different algorithms in Fig. 19. Fig. 19 shows the proposed algorithm has better detection result than the other algorithms. Table III shows the areas under ROC curves of different algorithms. The larger the area is, the better an algorithm is. From Table III, we can see that our algorithm has the largest area.

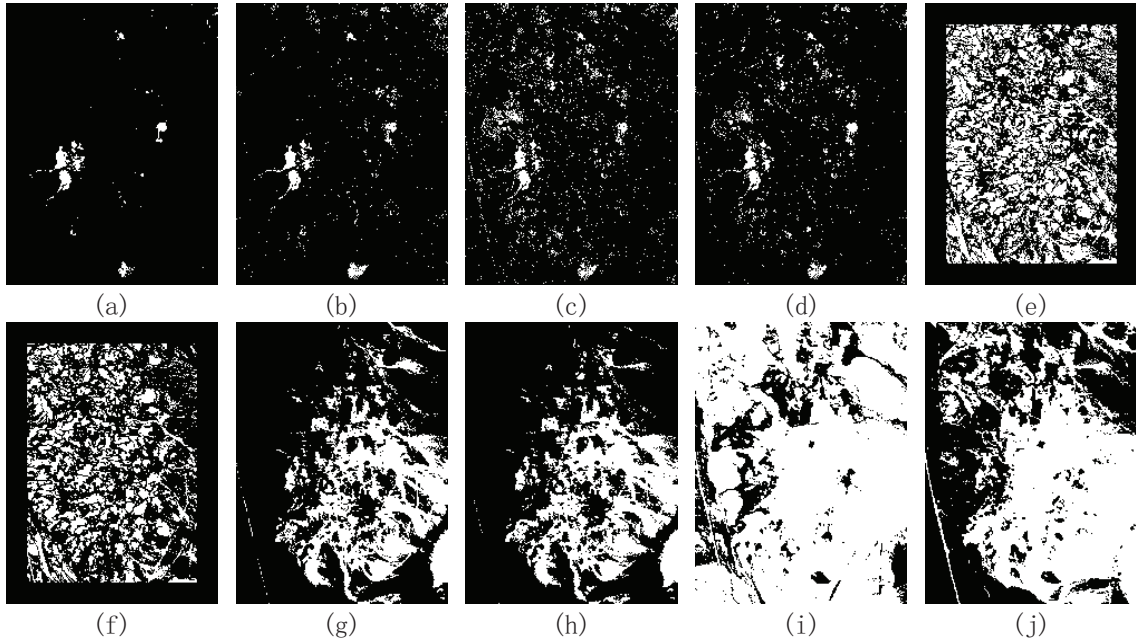


Fig. 18. The binary detection results of the AVIRIS hyperspectral image: (a) our algorithm, (b) CEM, (c) ACE, (d) AMF, (e) L-ACE, (f) L-AMF, (g) SAM, (h) SID, (i) LCMV-CBS-SAM (j) SVD-CEM. The probabilities of detection in (a)-(j) are all 0.5.

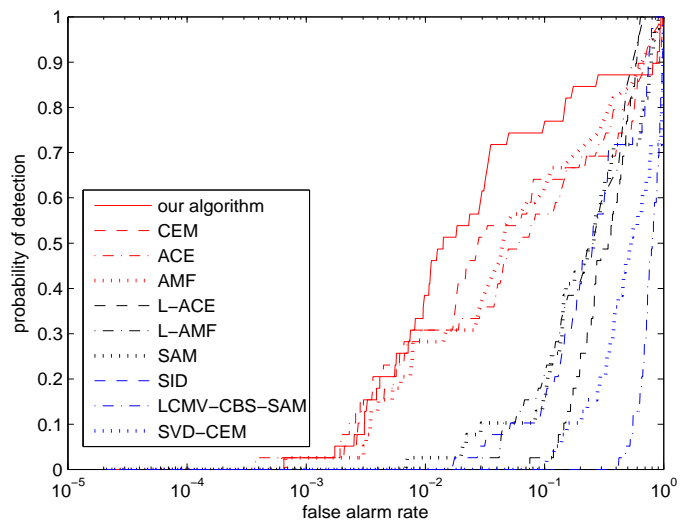


Fig. 19. ROC curves of different algorithms for the AVIRIS hyperspectral image.

TABLE III
THE AREAS UNDER ROC CURVES OF DIFFERENT ALGORITHMS FOR THE AVIRIS HYPERSPECTRAL IMAGE

	our algorithm	CEM	ACE	AMF	L-ACE	L-AMF	SAM	SID	LCMV-CBS-SAM	SVD-CEM
area	0.8519	0.7677	0.7900	0.8083	0.6486	0.7163	0.6615	0.6598	0.2109	0.4139

D. Real Hyperspectral Image Experiment 2

In this subsection, the hyperspectral mapper (HyMap) data sets obtained from the Rochester Institute of Technology (RIT) Hyperspectral Target Detection Blind Test website [38], [39] are used to conduct experiments. The website provides two data sets: a self test set and a blind test set. For the self test set, the website provides the ground truths of targets to users, while for the blind test set, the website reserves the ground truths and does not provide them to users. However, for the blind test set, utilizing the reserved ground truths, the website provides users with an online application which can score the uploaded detection results. A detection result's score is the number of pixels whose detection outputs are larger than or equal to the target location pixel's detection output. A perfect score is one meaning the target pixel has the largest detection output. The score in fact represents the number of false alarm pixels when the target is detected. Obviously, the smaller the score is, the better the detection result is. In this paper, we use both the self test set and the blind test set to do experiments. The HyMap images, both in calibrated spectral radiance and in spectral reflectance after atmospheric compensation, are available [38]. In our experiments, the images in spectral reflectance are used. The spectral signatures of targets used in the experiments are also provided by the website. The HyMap reflectance image provided by the website is scaled by 10000. In our experiments, we first divide the HyMap images by 10000, i.e., we use the unscaled data. For spectral signatures of targets, in order to make the magnitude similar with the HyMap image and make their magnitudes in the range of [0, 1], we divide the spectral signatures of targets by 100. The HyMap hyperspectral image has 126 bands with 280×800 pixels, and the spectral range is $0.45 - 2.5 \mu\text{m}$. After removing the low SNR and water absorption bands, 124 bands are used in the experiment. The scene is the small town of Cooke City, Montana, USA. The first band of the HyMap self test set is shown in Fig. 20.

There are three vehicle targets in the HyMap image called V1, V2 and V3. In this subsection, we detect all of these three vehicle targets using both the self test set and the blind test set. Since V1, V2 and V3 all occupy only one pixel, we cannot identify them in the image with our naked eyes. Fig. 21 shows the ground truth of V1, V2 and V3 in the self test set. Fig. 22 shows spectral signatures of V1, V2 and V3 used in the experiments. The website provides two distinctly different spectral signatures for V2, and we use the white truck's paint one. Fig. 23 shows V1, V2 and V3 located pixels' spectra in the self test set. From Fig. 22 and Fig. 23, we can see the spectral signatures of targets used in the experiment are very different with the targets located pixels' spectra. We first detect V1 using the self test set. The scores of our algorithm for V1 in the self test set under different ε are shown in Table IV. The scores of different algorithms for V1 in the self test set are shown in Table V. The ε used in our algorithm for V1 in Table V is that which has the best result for V1 in Table IV. Using the scores, we can



Fig. 20. The first band of the HyMap self test set.

calculate the corresponding false alarm rates. The corresponding false alarm rates are also shown in Table IV and Table V (shown in parentheses). The sizes of inner windows and outer windows for the L-ACE and the L-AMF are selected as follows: since the target occupy only one pixel and the size of inner window should be similar to the size of target [12], for the size of inner window, we try 1 or 3, and for the size of outer window, we try all the odd numbers in [1, 39]. Then we find that when the size of inner window is set to 3 and the size of outer window is set to 9, we get the best result for V1 in the self test set. Thus, in the following experiments for the other targets, for the L-ACE and the L-AMF, we set the size of inner window to 3 and set the size of outer window to 9 and report corresponding results. The output detection results of different algorithms for V1 in the self test set are shown in Fig. 24. Fig. 25 shows the binary detection results of different algorithms for V1 in the self test set when the probabilities of detection reach 1. For the results of our algorithm shown in Fig. 24 and Fig. 25, the ε is set to that which has the best result for V1 in Table IV. In Fig. 25, the false alarm pixels are those background pixels whose output values are equal to or larger than the output value of the target pixel. From Fig. 25, we can see the false alarm pixels of the proposed algorithm is much fewer than the other algorithms when the target is detected. We also show the scores of our algorithm under different ε for V2 and V3 in the self test set in Table IV. The scores of different algorithms for V2 and V3 in the self test set are shown in Table V. The ε used in our algorithm in Table V are those which have the best results for corresponding targets in Table IV. The corresponding false alarm rates are also shown in Table IV and Table V (shown in parentheses). In order to save space, we do not show the output detection results and binary detection results for targets V2 and V3 in the self test set as Fig. 24 and Fig. 25.

TABLE IV
THE SCORES AND FALSE ALARM RATES OF OUR ALGORITHM FOR THE HYMAP SELF TEST SET UNDER DIFFERENT ε

ε	10^{-1}	10^{-2}	10^{-3}	10^{-4}	10^{-5}	10^{-6}
V1	3208 (0.01432)	3658 (0.01633)	4327 (0.01931)	4408 (0.01967)	4413 (0.01970)	4415 (0.01971)
V2	2122 (0.00947)	42035 (0.18765)	53901 (0.24063)	55223 (0.24653)	55354 (0.24711)	55369 (0.24718)
V3	8413 (0.03755)	3170 (0.01415)	2893 (0.01291)	2871 (0.01281)	2863 (0.01278)	2862 (0.01277)

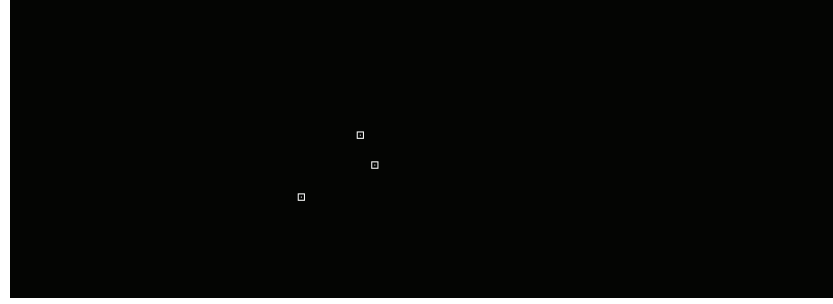


Fig. 21. The ground truth of the targets V1, V2 and V3 in the HyMap self test set. The bright point in the middle square is the location of V1, and the bright point in the right square is the location of V2, and the bright point in the left square is the location of V3.

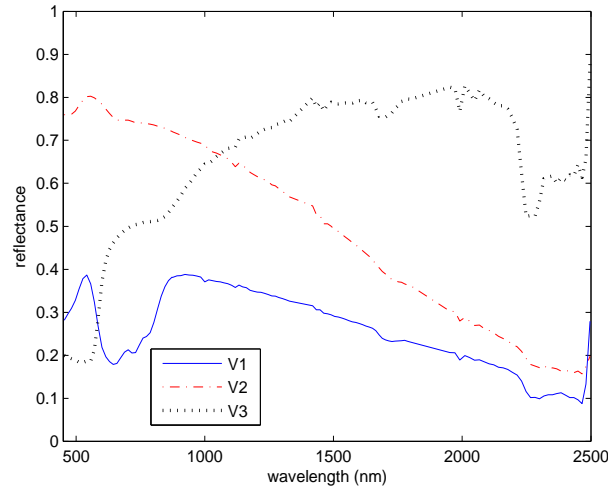


Fig. 22. Spectral signatures of targets used in the HyMap hyperspectral image experiment.

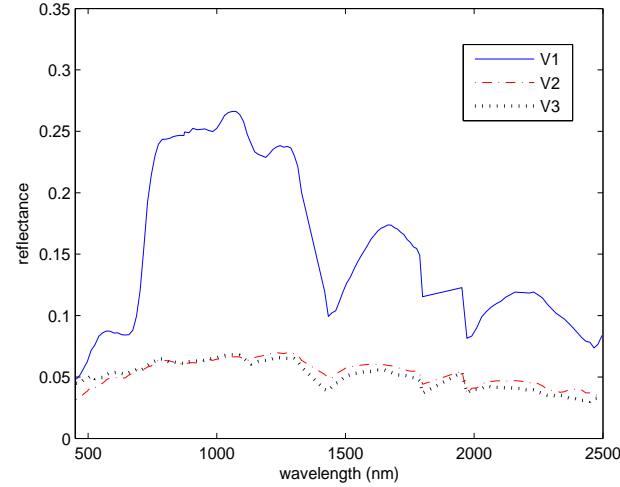


Fig. 23. Targets located pixels' spectra in the HyMap self test set.

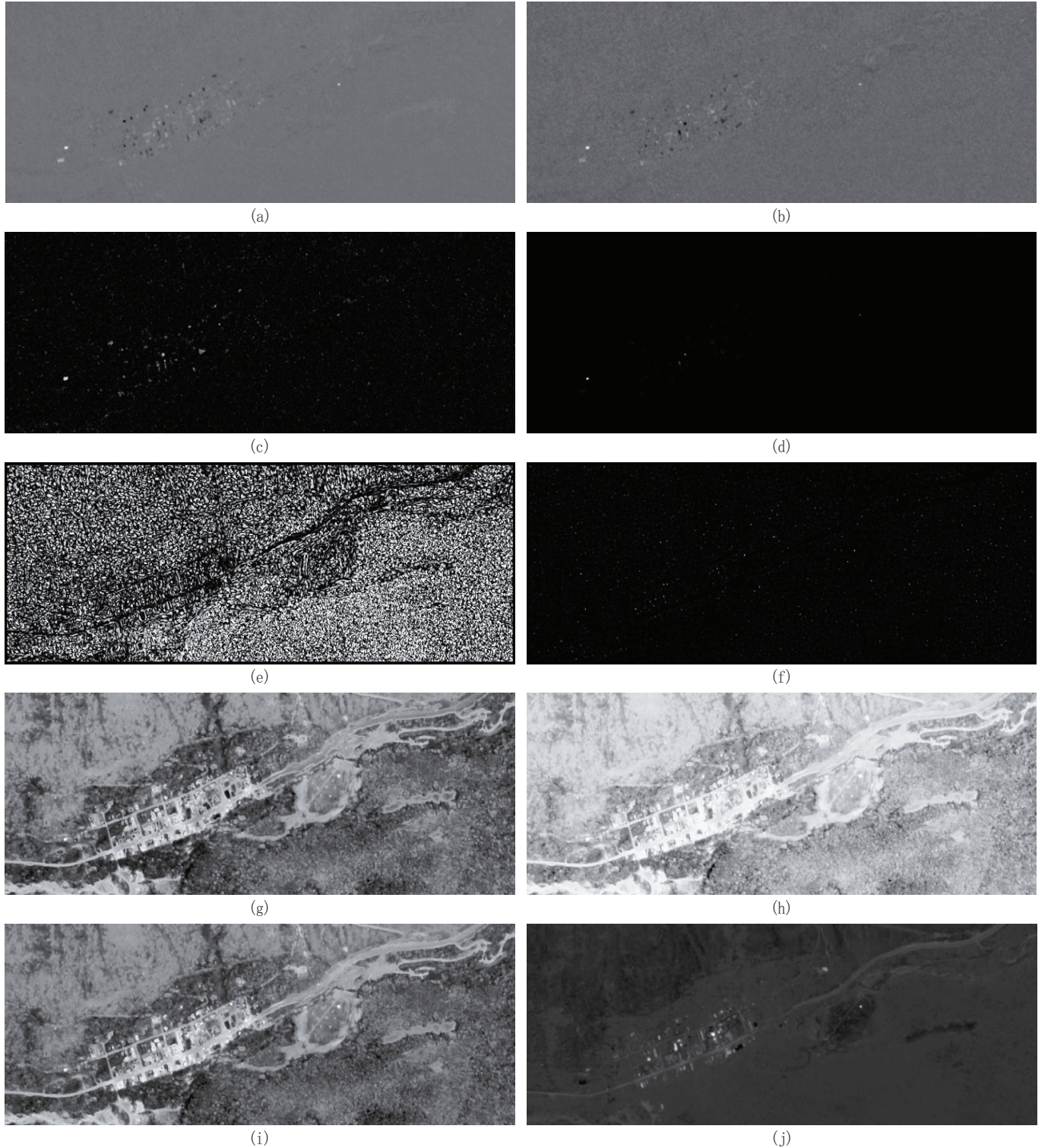


Fig. 24. The output detection results of V1 in the HyMap self test set: (a) our algorithm, (b) CEM, (c) ACE, (d) AMF, (e) L-ACE, (f) L-AMF, (g) SAM, (h) SID, (i) LCMV-CBS-SAM (j) SVD-CEM.

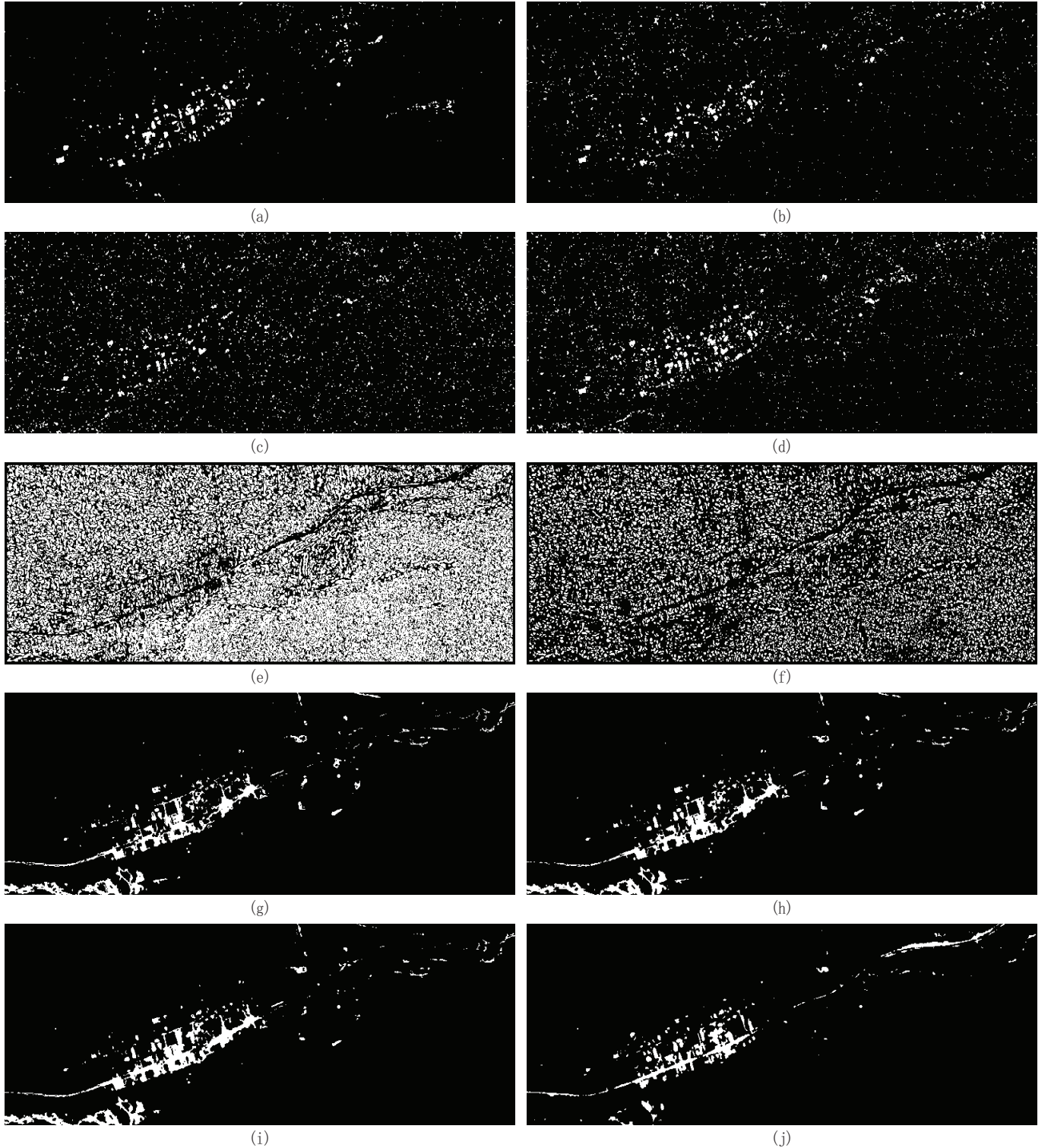


Fig. 25. The binary detection results of V1 in the HyMap self test set: (a) our algorithm, (b) CEM, (c) ACE, (d) AMF, (e) L-ACE, (f) L-AMF, (g) SAM, (h) SID, (i) LCMV-CBS-SAM (j) SVD-CEM. The probabilities of detection in (a)-(j) are all 1.

TABLE V
THE SCORES AND FALSE ALARM RATES OF DIFFERENT ALGORITHMS FOR THE HYMAP SELF TEST SET

target	our algorithm	CEM	ACE	AMF	L-ACE	L-AMF	SAM	SID	LCMV-CBS-SAM	SVD-CEM
V1	3208 (0.01432)	4415 (0.01971)	7970 (0.03558)	8225 (0.03671)	124547 (0.55601)	57444 (0.25644)	8252 (0.03683)	8068 (0.03601)	8664 (0.03867)	5793 (0.02586)
	2122 (0.00947)	55372 (0.24719)	111212 (0.49648)	97822 (0.43670)	82313 (0.36746)	93219 (0.41615)	2278 (0.01017)	2362 (0.01054)	2237 (0.00998)	14047 (0.06271)
V3	2862 (0.01277)	2862 (0.01277)	4061 (0.01813)	4343 (0.01938)	129741 (0.57920)	120324 (0.53716)	20747 (0.09262)	23390 (0.10442)	27343 (0.12206)	19445 (0.08680)

We also use the blind test set to do experiments. We show the scores of our algorithm under different ε for V1, V2 and V3 in the blind test set in Table VI using the online application provided by the website. Table VII shows the scores of different algorithms for V1, V2 and V3 in the blind test set. The ε used in our algorithm in Table VII are those which have the best results for corresponding targets in Table VI. The corresponding false alarm rates are also shown in Table VI and Table VII (shown in parentheses).

The experiment results show that overall our algorithm obtains better results than the other algorithms for the HyMap data sets. Our algorithm is based on CEM. The experiment results show our algorithm at least can obtain the same result with CEM. In fact, in most cases our algorithm performs better than CEM. Our algorithm obtains better results than CEM, except that for the V3 in the self test set and V2 in the blind test set our algorithm has the same results with CEM. This shows that our algorithm can improve the performance of CEM. From Table V and Table VII, we can see that for different targets both in the self test set and in the blind test set, our algorithm has the best results among different algorithms, except for the V3 in the blind test set. For V3 in the blind test set, L-ACE, L-AMF and SVD-CEM perform better than our algorithm. Although L-ACE, L-AMF and SVD-CEM have better results than our algorithm for V3 in the blind test set, for the other targets, these algorithms perform much worse than our algorithm and do not have good results. These algorithms only obtain better results for this one target. In fact, no one algorithm always has the best results for all the targets. Our algorithm has the best results for all targets except for the V3 in the blind test set, and obtains the best results in more cases than the other algorithms, thus we can conclude that overall our algorithm performs better than the other algorithms for the HyMap data sets.

TABLE VI
THE SCORES AND FALSE ALARM RATES OF OUR ALGORITHM FOR THE HYMAP BLIND TEST SET UNDER DIFFERENT ε

ε	10^{-1}	10^{-2}	10^{-3}	10^{-4}	10^{-5}	10^{-6}
V1	715 (0.00319)	401 (0.00179)	416 (0.00185)	422 (0.00188)	422 (0.00188)	422 (0.00188)
V2	1211 (0.00540)	907 (0.00404)	855 (0.00381)	845 (0.00377)	843 (0.00376)	843 (0.00376)
V3	4147 (0.01851)	3306 (0.01475)	3298 (0.01472)	3298 (0.01472)	3301 (0.01473)	3302 (0.01474)

Next we analyze the effect of the using of ε . We plot ROC curves of the proposed algorithm using different values of ε for the AVIRIS hyperspectral image in Fig. 26. The ROC curve of CEM is also given in Fig. 26. The

TABLE VII
THE SCORES AND FALSE ALARM RATES OF DIFFERENT ALGORITHMS FOR THE HYMAP BLIND TEST SET

target	our algorithm	CEM	ACE	AMF	L-ACE	L-AMF	SAM	SID	LCMV-CBS-SAM	SVD-CEM
V1	401 (0.00179)	422 (0.00188)	477 (0.00213)	787 (0.00351)	138319 (0.61749)	73314 (0.32729)	10065 (0.04493)	6699 (0.02990)	5194 (0.02318)	4055 (0.01810)
	843 (0.00376)	843 (0.00376)	2118 (0.00945)	1470 (0.00656)	68687 (0.30663)	54094 (0.24149)	2683 (0.01197)	2487 (0.01110)	2129 (0.00950)	1939 (0.00865)
V3	3298 (0.01472)	3302 (0.01474)	5581 (0.02491)	5528 (0.02467)	621 (0.00277)	1286 (0.00574)	12333 (0.05505)	12105 (0.05404)	12952 (0.05782)	2129 (0.00950)

scores of the proposed algorithm using different values of ε for the HyMap self test set and the blind test set are given in Table IV and Table VI, respectively. In Fig. 26, the ROC curve of $\varepsilon = 0$ and CEM are overlapped. This is not surprise, because when ε is set to 0, the proposed algorithm equals CEM. In fact, CEM can be seen as a special case of the proposed algorithm. This result also verifies that using the barrier method, we can obtain the same detection result with CEM if ε is set to 0. In Fig. 26, the ROC curve of $\varepsilon = 10^{-3}$ is almost overlapped with the ROC curves of $\varepsilon = 0$ and CEM. In the two synthetic hyperspectral image experiments and the AVIRIS hyperspectral image experiment, we always set ε to 0.1, and can get good results. However, in the HyMap data sets experiments, for different targets, our algorithm obtains the best results under different ε . This may due to the fact that the degree of spectral variation for different targets in the HyMap data sets are very different. Thus our algorithm becomes more sensitive to ε . For the two synthetic hyperspectral images and the AVIRIS hyperspectral image, we all set ε to 0.1 for our algorithm, and obtain the best results among different algorithms. Especially, for the synthetic hyperspectral image 1, although we add random vectors which have unity norms to the endmember A, we can also get good results when we set ε to 0.1. This suggests that our algorithm is robust to ε to some extent. The optimal value of ε may be relevant to the magnitude of the used spectral signature of target, the spectral variation degree and the noise. How to determine the optimal value of ε will be a topic of our future research.

E. Discussion and Future Work

We use two synthetic hyperspectral images and two real hyperspectral images to conduct experiments. For the synthetic hyperspectral image 1, we simulate the spectral variability of target. The detection results show our proposed algorithm is more robust and performs better than the other algorithms. In synthetic hyperspectral image 2, there is no pure pixel. The mixed pixel can cause the target spectral variation. The experiment results show the proposed algorithm is more robust than the other algorithms under such circumstance. For the AVIRIS hyperspectral image, we plot the spectra of target pixels which demonstrate that in real hyperspectral image there indeed exists target spectral variability. The proposed algorithm uses an inequality constraint to guarantee that the outputs of target spectra varying in a certain set are larger than 1, thus even target spectra have some spectral variation, these target spectra can still be detected. So the proposed algorithm is more robust to the target spectral variability. The experiment results demonstrate the proposed algorithm obtains better results than the other algorithms for the

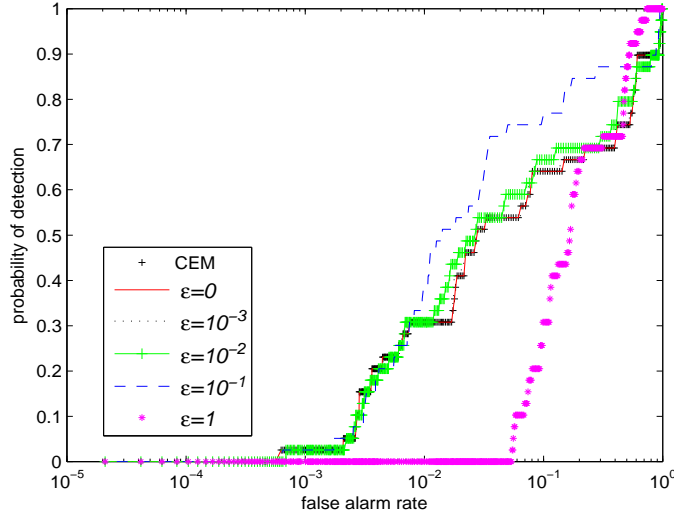


Fig. 26. ROC curves of the proposed algorithm using different values of ϵ for the AVIRIS hyperspectral image.

AVIRIS hyperspectral image. In the HyMap data sets experiments, the spectral signatures of targets used are very different with the spectra of the target pixels. The variation between the spectral signatures of targets and the target pixels' spectra need to be detected makes the detection difficult. Although our algorithm does not obtain the best result for every target, our algorithm performs best for most of the target. Except for V3 in the blind test set, our algorithm obtains the best results for the other targets. L-ACE, L-AMF and SVD-CEM have better results than our algorithm for V3 in the blind test set, but for the other targets, these algorithms perform worse than our algorithm and do not have good results. These algorithms only obtain better results for this one target. Thus, overall our algorithm performs best among different algorithms for the HyMap data sets. Our future work will focus on how to determine the optimal value of the parameter ϵ in our algorithm. Another topic of our future research will be applying the dual window technology to our algorithm as that used in L-ACE and L-AMF. The dual window technology can make use of the local statistic character of the data, which may lead to better results.

V. CONCLUSION

In the real hyperspectral image, there is inherent spectral variability within target. The spectral variability is one of the major obstacles for successful target detection. In this paper, we propose a robust hyperspectral image target detection algorithm. The proposed algorithm transforms target detection to a convex optimization problem and uses a kind of interior point method named barrier method to solve the formulated optimization problem. The experiment results show the proposed algorithm is more robust to target spectral variability and gets better detection results than other classical algorithms.

ACKNOWLEDGMENT

The authors would like to thank the handling editor and all anonymous reviewers who provided insightful and helpful comments.

REFERENCES

- [1] D. Manolakis, D. Marden, and G. A. Shaw, "Hyperspectral image processing for automatic target detection applications," *Lincoln Lab. J.*, vol. 14, no. 1, pp. 79-116, 2003.
- [2] D. Manolakis and G. Shaw., "Detection algorithms for hyperspectral imaging applications," *IEEE Signal Process. Mag.*, vol. 19, no. 1, pp. 29-43, Jan. 2002.
- [3] G. A. Shaw and H. K. Burke, "Spectral imaging for remote sensing," *Lincoln Lab. J.*, vol. 14, no. 1, pp. 3-28, 2003.
- [4] E. M. Winter, M. Miller, C. Simi, A. Hill, T. Williams, D. Hampton, M. Wood, J. Zadnick, and M. Sviland, "Mine detection experiments using hyperspectral sensors," in *Proc. SPIE Int. Soc. Opt. Eng.*, Orlando, FL, United States, 2004, pp. 1035-1041.
- [5] M. T. Eismann, A. D. Stocker, and N. M. Nasrabadi, "Automated hyperspectral cueing for civilian search and rescue," *Proc. IEEE*, vol. 97, no. 6, pp. 1031-1055, Jun. 2009.
- [6] R. S. DiPietro, E. Truslow, D. G. Manolakis, S. E. Golowich, and R. B. Lockwood, "False-alarm characterization in hyperspectral gas-detection applications," in *Proc. SPIE Int. Soc. Opt. Eng.*, San Diego, CA, United States, 2012.
- [7] F. C. Robey, D. R. Fuhrmann, E. J. Kelly, and R. Nitzberg, "A CFAR adaptive matched filter detector," *IEEE Trans. Aerosp. Electron. Syst.*, vol. 28, no. 1, pp. 208-218, Jan. 1992.
- [8] W. Chen and I.S. Reed, "A new CFAR detection test for radar," *Digital Signal Processing*, vol. 1, no. 4, pp. 198-214, 1991.
- [9] D. Manolakis, R. Lockwood, T. Cooley, and J. Jacobson, "Is there a best hyperspectral detection algorithm?" in *Proc SPIE*, Orlando, USA, 2009.
- [10] S. Kraut and L. L. Scharf, "The CFAR adaptive subspace detector is a scale-invariant GLRT," *IEEE Trans. Signal Process.*, vol. 47, no. 9, pp. 2538-2541, Sept. 1999.
- [11] S. Kraut, L. L. Scharf, and L. T. McWhorter, "Adaptive subspace detectors," *IEEE Trans. Signal Process.*, vol. 49, no. 1, pp. 1-16, Jan. 2001.
- [12] S. Matteoli, M. Diani, and G. Corsini, "A tutorial overview of anomaly detection in hyperspectral images," *IEEE Aerosp. Electron. Syst. Mag.*, vol. 25, no. 7, pp. 5-28, Jul. 2010.
- [13] W. H. Farrand and J. C. Harsanyi, "Mapping the distribution of mine tailings in the Couer d'Alene River valley, Idaho, through the use of a constrained energy minimization technique," *Remote Sens. Environ.*, vol. 59, no. 1, pp. 64-76, Jan. 1997.
- [14] J. C. Harsanyi, Detection and classification of subpixel spectral signatures in hyperspectral image sequences, Ph.D. dissertation, University of Maryland Baltimore County, 1993.
- [15] F. A. Kruse, A. B. Lefkoff, J. W. Boardman, K. B. Heidebrecht, A. T. Shapiro, P. J. Barloon, and A. F. H. Goetz, "The spectral image processing system (SIPS) - Interactive visualization and analysis of imaging spectrometer data," *Remote Sens. Environ.*, vol. 44, pp. 145-163, 1993.
- [16] C.-I. Chang, "An information-theoretic approach to spectral variability, similarity, and discrimination for hyperspectral image analysis," *IEEE Trans. Inform. Theory*, vol. 46, no. 5, pp. 1927-1932, Aug. 2000.
- [17] Q. Du, H. Ren, and C.-I. Chang, "A comparative study for orthogonal subspace projection and constrained energy minimization," *IEEE Trans. Geosci. Remote Sens.*, vol. 41, no. 6, pp. 1525-1529, Jun. 2003.
- [18] J. C. Harsanyi and C.-I. Chang, "Hyperspectral image classification and dimensionality reduction: An orthogonal subspace projection approach," *IEEE Trans. Geosci. Remote Sens.*, vol. 32, no. 4, pp. 779-785, Jul. 1994.
- [19] Y. Chen, N. M. Nasrabadi, and T. D. Tran, "Sparse representation for target detection in hyperspectral imagery," *IEEE J. Sel. Top. Sign. Proces.*, vol. 5, no. 3, pp. 629-640, Jun. 2011.
- [20] Y. Chen, N. M. Nasrabadi, and T. D. Tran, "Simultaneous joint sparsity model for target detection in hyperspectral imagery," *IEEE Geosci. Remote Sens. Lett.*, vol. 8, no. 4, pp. 676-680, Jul. 2011.
- [21] A. M. Bruckstein, D. L. Donoho and M. Elad, From sparse solutions of systems of equations to sparse modeling of signals and images, *Siam Review*, Society for Industrial and Applied Mathematics, vol. 51, no. 1, pp. 34-81, 2009.

- [22] C.-I. Chang and S. Wang, "Constrained band selection for hyperspectral imagery," *IEEE Trans. Geosci. Remote Sens.*, vol. 44, no. 6, pp. 1575-1585, Jun. 2006.
- [23] C.-I. Chang and Q. Du, "Estimation of number of spectrally distinct signal sources in hyperspectral imagery," *IEEE Trans. Geosci. Remote Sens.*, vol. 42, no. 3, pp. 608-619, Mar. 2004.
- [24] L. L. Scharf, *Statistical Signal Processing, Detection Estimation and Time Series Analysis*. Reading, MA: Addison-Wesley, 1991.
- [25] S. A. Vorobyov, A. B. Gershman, and Z.-Q. Luo, "Robust adaptive beamforming using worst-case performance optimization: a solution to the signal mismatch problem," *IEEE Trans. Signal Process.*, vol. 51, no. 2, pp. 313-324, Feb. 2003.
- [26] S. Boyd and L. Vandenberghe, *Convex Optimization*. Cambridge, U.K.: Cambridge Univ. Press, 2004.
- [27] J. Nocedal and S. J. Wright, *Numerical Optimization*. New York, USA: Springer, 2000.
- [28] C.-I. Chang, "Multiparameter receiver operating characteristic analysis for signal detection and classification," *IEEE Sensors J.*, vol. 10, no. 3, pp. 423-442, Mar. 2010.
- [29] J. Kerekes, "Receiver operating characteristic curve confidence intervals and regions," *IEEE Geosci. Remote Sens. Lett.*, vol. 5, no. 2, pp. 251-255, Apr. 2008.
- [30] N. M. Nasrabadi, "Regularized spectral matched filter for target recognition in hyperspectral imagery," *IEEE Signal Process. Lett.*, vol. 15, pp. 317-320, 2008.
- [31] Y. Zhang, B. Du, and L. Zhang, "Regularization framework for target detection in hyperspectral imagery," *IEEE Geosci. Remote Sens. Lett.*, vol. 11, no. 1, pp. 313-317, 2014.
- [32] Y.-C. C. Chang, H. Ren, C.-I. Chang, and R. S. Rand, "How to design synthetic images to validate and evaluate hyperspectral imaging algorithms," in *Proc. SPIE Int. Soc. Opt. Eng.*, Orlando, FL, United States, 2008.
- [33] J. B. Adams, M. O. Smith, and A. R. Gillespie, *Remote Geochemical Analysis: Elemental and Mineralogical Composition*. Cambridge, U.K.: Cambridge University Press, 1993.
- [34] L. Miao and H. Qi, "Endmember extraction from highly mixed data using minimum volume constrained nonnegative matrix factorization," *IEEE Trans. Geosci. Remote Sens.*, vol. 45, no. 3, pp. 765-777, Mar. 2007.
- [35] R. N. Clark, G. A. Swayze, A. J. Gallagher, T. V. V. King, and W. M. Calvin, "The U.S. geological survey digital spectral library: Version 1: 0.2 to 3.0 microns," *U.S. Geological Survey, Denver, CO, Open File Rep.*, pp. 93-592, 1993.
- [36] AVIRIS Cuprite data set. [Online]. Available: <http://aviris.jpl.nasa.gov/html/aviris.freedata.html>
- [37] USGS map of the distribution of different minerals in the Cuprite mining district in Nevada. [Online]. Available: <http://speclab.cr.usgs.gov/PAPERS/tetracorder/>
- [38] D. Snyder, J. Kerekes, I. Fairweather, R. Crabtree, J. Shive, and S. Hager, "Development of a web-based application to evaluate target finding algorithms," in *Proc. IEEE Int. Geosci. Remote Sens. Symp.*, Boston, MA, United States, 2008, pp. II915-II918.
- [39] J. Kerekes and D. Snyder. Target Detection Blind Test. [Online]. Available: <http://dirsapps.cis.rit.edu/blindtest/>